To appear in:

Journal of Theoretical and Applied Physics

Online ISSN: 2251-7235 **Print ISSN: 2251-7227**

Received: 30 September 2025

Revised: 20 December 2025

Accepted: 09 April 2026

DOI: https://doi.org/10.57647/jtap.2026.2004.09

Research Article

Investigation of Photon Interaction Parameters of Perovskite Ceramics Materials using Phy-X/PSD And NGCal Software

Muhammed Abdurraheem[1*], Wasiu Yahya[1,2], Sunday Ajani[1], Godwin Egbeyale[1]

[1]*Department of Physics and Materials Science, Kwara State University, Malete, Kwara, Nigeria*
[2]*Department of Physics, University, Ilorin, Ilorin, Kwara, Nigeria*

***Corresponding author:** abdurraheemlayimuhammed@gmail.com

ORCID: https://orcid.org/0009-0000-6735-2762

Abstract

This study aims to evaluate the radiation shielding performance of selected metal oxide–based and oxide double perovskite ceramic materials using various photon attenuation parameters. The photon attenuation parameters were calculated and analyzed using Phy-X/PSD and NGCal software over the range of 0.015–15 MeV. The results, based on the total interaction cross-section of photon–matter interactions, show that all investigated samples exhibit higher attenuation efficiency in the low-energy region due to the dominance of the photoelectric effect, followed by a gradual reduction in shielding performance in the intermediate and high-energy regions, where Compton scattering and pair production prevail. Materials with higher atomic number (Z) and greater density demonstrate superior shielding performance, as reflected by higher MAC and LAC values and lower HVL, TVL, and MFP values. The radiation

shielding parameters obtained from the two software tools were in good agreement, with differences within 0.1%. Overall, both perovskite families display promising radiation shielding capabilities, with oxide double perovskite samples showing enhanced attenuation efficiency compared to metal oxide–based perovskite composites, highlighting their greater potential for effective photon radiation shielding applications.

Keywords: Perovskite, Radiation shielding, Oxide double perovskite, Metal oxide-based perovskite, Mass attenuation coefficient

Introduction

The use of ionizing photon radiation has significantly contributed to various medical applications, including medical imaging, industrial radiography, medical research laboratories, diagnostic imaging, and cancer treatment [1, 3]. However, inadvertent exposure to these photon energies has created a demand for effective shielding materials to protect patients [1, 6], medical staff, sensitive equipment, and individuals in the surrounding environment [1], while ensuring that the doses received do not exceed the permissible limits for patients, workers, or the public [2]. Moreover, researchers have investigated various materials for radiation shielding to protect life and the surrounding environment from the effects of photon radiation [4, 5]. Conventional shielding materials, such as lead, have long been used due to their high density, effective radiation attenuation, low cost, and high atomic number (Z). However, in nuclear facilities, thick concrete is also employed as a radiation barrier, but it has notable drawbacks [1]. Lead is highly toxic, heavy, bulky, mechanically rigid, and environmentally hazardous, with chronic exposure leading to serious health problems [1, 6, 7, 10]. Similarly, concrete shields must be quite thick and completely opaque, obstructing visibility, but deteriorate over time under intense radiation [1]. These limitations highlight the urgent need for alternative shielding materials that are environmentally safe, lightweight, high-density, and possess strong mechanical properties [1, 6, 10]. In recent years, various materials have been proposed and studied for radiation shielding, including polymers, glass [6, 7], and perovskite ceramics [8, 9]. Among these novel materials, perovskite ceramics have gained significant attention as potential candidates for radiation protection due to their unique

crystal structure, high density, high atomic number, thermal and chemical stability, non-toxicity, resistance to oxidation, low thermal expansion, lightweight nature, durability, environmental friendliness [6, 10, 11], high radiation absorption capability, mechanical strength, and excellent structural stability. These properties enable perovskite ceramics to maintain their integrity under high radiation exposure, making them suitable for long-term use in nuclear medicine and engineering applications [11]. In this study, a computational approach was employed to provide a reliable pathway to predict and analyze photon radiation shielding performance of perovskite ceramics theoretically.

Oxide-based perovskites have the general chemical formula ABO_3, and doping involves substituting atoms at either the A-site (e.g., Ba or Sr) or the B-site (e.g., Ti or Mn) with appropriate dopants. Doping at the A-site primarily alters the ionic size, induces lattice distortions, and modifies the material density, whereas doping at the B-site affects charge compensation, bandgap tuning, and magnetic ordering. Incorporating high-Z metals (e.g., Mo) or oxide-based metals (e.g., ZrO_2, TeO) enhances photon absorption by increasing the probability of photon–matter interactions. However, high-Z dopants typically have larger atomic weights, which increases the overall density of the material and consequently reduces photon penetration depth. In contrast, oxide double perovskites are rock-salt crystal structure with the general chemical formula $A_2BB'O_6$, where A represents a larger cation (e.g., Ba^{2+}, La^{3+}) and B/B′ represent smaller transition metal cations (e.g., Fe, Re, Mn, Nb, Mo, Ni, Y). This structure is a modified perovskite lattice with ordered B-site cations, enabling precise tuning of structural, electronic, magnetic, and optical properties. The flexibility to substitute different cations at the A, B, or B′ sites allows researchers to design materials with tailored properties for specific applications [9]. Hence, metal oxide–based and oxide double perovskites have recently attracted significant attention due to their compositional flexibility, structural and functional properties, and potential for enhanced photon–matter interactions. However, despite these advantages, their potential applications and characteristics as radiation shielding materials have not been thoroughly explored, particularly across a wide photon energy range. Incorporating heavy metal oxides into perovskite matrices can increase photon interaction probabilities, thereby improving their attenuation performance.

Moreover, research on lead-free $BaTiO_3$ (BTO) perovskite ceramics doped with ZnO, SiO_2, and WO_3 oxides and synthesized via the solid-state reaction process [12] found that the addition of ZnO and WO_3 to $BaTiO_3$ enhanced the linear attenuation coefficient (LAC) values, whereas the addition of SiO_2 reduced both the density and shielding capacity of the fabricated BTO. Another study on the structural and radiation shielding properties of selected perovskite ceramics ($BaTiO_3$ and $SrMnO_3$) doped with ZrO_2, Mo, ZnO, and TeO_2 using the solid-state reaction method [9] reported that the $BaTiO_3 - ZrO_2$ sample exhibited excellent gamma-ray attenuation, while $SrMnO_3 - TeO_2$ was effective for neutron shielding. Although numerous studies have been published on double perovskites but no systematic study has explored the photon interaction or radiation-shielding parameters of the selected double perovskite materials.

Materials and Methods

Two classes of perovskite materials were selected for this study: metal oxide–based perovskites ($BaTiO_3 - ZrO_2$, $BaTiO_3 - Mo$, $SrMnO_3 - TeO_2$, $SrMnO_3 - ZnO$) and oxide double perovskites (Ba_2FeReO_6, Ba_2NaNbO_6, Ba_2YMoO_6, La_2NiMnO_6 La_2FeMnO_6). Their photon radiation shielding parameters, including mass attenuation coefficient (MAC), linear attenuation coefficient (LAC), half-value layer (HVL), tenth-value layer (TVL), and mean free path (MFP) [10, 11], were investigated over a photon energy range of 0.015–15 MeV using Phy-X/PSD [13, 14] and NGCal software [15]. This energy range was selected because it covers the three dominant photon–matter interaction mechanisms: photoelectric effect (0–0.1 MeV), Compton scattering (0.1–2 MeV), and pair production (3–15 MeV), which primarily determine the radiation shielding performance of materials. By encompassing all these interaction regimes, the study provides a comprehensive analysis and allows for results that are comparable to international standards, facilitating the accurate modeling and design of effective perovskite-based shielding solutions [16].

The intensity of a photon beam decreases as it passes through an absorbing material due to dominant photon–matter interaction processes such as the photoelectric effect, Compton scattering, and pair production. These interactions result in the transfer of energy from the incident photons to the atomic electrons of the absorbing material. The decrease in radiation intensity during this interaction is stated by Lambert-Beer's law as given in equation (1) [17]:

$$I\,(x) = I_0 e^{-\mu x}, \quad (1)$$

where I(x) is the transmitted intensity, I_0 is the incident intensity μ is the linear attenuation coefficient of the material and x is the thickness of the material.

Linear attenuation coefficient (LAC)

This property characterizes how effectively a material attenuates a photon beam per unit thickness. It depends on the atomic composition and density of the material, as well as the energy of the incident photons [9, 13, 18]. LAC is obtained from the Lambert-Beer's law as expressed in equation (2) [19, 20]:

$$\mu = -ln\left(\frac{I}{I_0}\right).\frac{1}{x}. \quad (2)$$

Mass Attenuation Coefficient (MAC)

This parameter measures the effectiveness of a material in attenuating photon radiation per unit mass. It is independent of material density but strongly depends on the atomic number of the constituent elements and the energy of the incident photons. It is expressed in equation (3) as [21]:

$$\mu_m = -\frac{1}{\rho x}.\, ln\left(\frac{I}{I_0}\right). \quad (3)$$

The relationship between LAC and MAC is given as equation (4) [22]:

$$\mu = \mu_m \times \rho, \quad (4)$$

where ρ is the density of material and μ_m is the mass attenuation coefficient

In case of a multi-element material such as chemical compound or homogeneous mixture establishing the sample, the MAC can be acquired from weighted sum of the coefficient for the elements as expressed in equation (5) [21, 22]:

$$\left(\frac{\mu}{\rho}\right)_{i\ compound} = \sum_i w_i \left(\frac{\mu}{\rho}\right)_i. \quad (5)$$

where $\left(\frac{\mu}{\rho}\right)_i$ is the MAC for the i-th constituent, w_i is the weight fraction for the i-th element, and is given as equation (6) [5]:

$$w_i = \frac{n_i A_i}{M}, \quad (6)$$

where n_i is the number of atoms of i-th element in the compound, A_i is the atomic mass of the compound in g/mol and M = $\sum n_i A_i$ and is the molar mass of the compound in g/mol.

Half Value Layer (HVL)

This is the thickness (in cm) of a shielding material required to reduce the intensity of a given photon to half of its original [17, 23]. It gives information about the thicknesses of a material that are suitable for radiation shielding. The lower the HVL value of the material is, the better its shielding ability against hazardous radiation [24]. It and can be expressed as equation (7) [9]:

$$\mathrm{HVL} = \frac{\ln 2}{\mu}. \quad (7)$$

Since $ln\ 2 \approx 0.693$

$$\mathrm{HVL} = \frac{0.693}{\mu}. \quad (8)$$

Tenth Value Layer (TVL)

This is the thickness (in cm) of a shielding material required to reduce the intensity of a given photon to tenth of its original, and can be expressed as equation (9) [17, 18]:

$$\mathrm{TVL} = \frac{\ln 10}{\mu}. \quad (9)$$

Since $ln\ 2 \approx 2.303$

$$\mathrm{TVL} = \frac{2.303}{\mu}. \quad (10)$$

Therefore, HVL and TVL are related by equation (11):

$$\mathrm{TVL} \approx 3.32 \times \mathrm{HVL}. \quad (11)$$

This is indicating that TVL is approximately 3.32 times the HVL. Thus, each TVL provides significantly more attenuation.

Mean Free Path (MFP)

This is average distance a unit photon can travel in a material without having any kind of interaction [18]. It is the average distance a photon can travel in a barrier before colliding [21]. It is obtained follow the Lambert-Beer's law as expressed in equation (12) [5]:

$$\lambda = \frac{1}{\mu}.$$

(12)

or

$$\lambda = \frac{1}{\mu} = \frac{1}{\left(\frac{\mu}{\rho}\right)\rho}.$$

(13)

Atomic Cross-section (ACS)

This represents the effective area of an atom that interacts with photon via photoelectric effect, Compton scattering and pair production [13]. It can be obtained as equation as (14) [19]:

$$\sigma_a = \frac{\mu}{\rho} \times \frac{A}{N_A},$$

(14)

where N_A is the Avogadro's number ($6.022 \times 10^{23} atoms/mol$), A is the atomic weight of the shielding material (g/mol), σ_a is the atomic cross section and ρ is the density of the material.

However, atomic cross section can also be expressed as equation (15) [22]:

$$\sigma_a = \frac{1}{N_A} \sum_i f_i A_i \left(\frac{\mu}{\rho}\right)_i,$$

(15)

where A_i is the atomic weight of every element in the target, $\left(\frac{\mu}{\rho}\right)_i$ is the MAC of the i-th element in cm^2/g and f_i is the fractional abundance of the i-th element.

Electronic Cross-section (ECS)

This represents the probability of interaction between a photon of radiation and the electrons within a material. It is the effective interaction area per electron, and primarily depending on the electron density of the material and the energy of the radiation [13]. It is expressed as equation (15):

$$\sigma_{el} = \frac{\mu}{\rho} \times \frac{A}{Z\,N_A},$$

(16)

where Z is the atomic number and σ_{el} is the electron cross section.

Electronic cross section can also be expressed as equation (17) [14]:

$$\sigma_{el} = \frac{1}{N_A} \sum_i \left(\frac{\mu}{\rho}\right)_i \frac{f_i\, w\, A_i}{Z_i},$$

(17)

where $f_i = \frac{n_i}{\sum_i n_i}$ and is the fractional abundance of the i-th element, and Z_i is the target element's atomic number.

Effective Atomic Number (Z_{eff})

This is calculated from the atomic numbers and proportions of constituent elements in a compound or mixture. It reflects how electrons in the material respond to incoming radiation. Materials with higher Z-elements tend have higher Z_{eff}. It is expressed as equation (18) [18]:

$$Z_{eff} = \frac{\sigma_{t,a}}{\sigma_{t,el}}, \quad (18)$$

where $\sigma_{t,a}$ is the total atomic cross section and $\sigma_{t,el}$ is the total electron cross section.

Effective Electron Density (N_{eff})

This is the number of electrons present per unit mass of a material [25]. It is dependent on both chemical compositions of the materials and incident photon energy for complex materials [14]. The higher the electron density, the better the material will shield radiation, and can be expressed as equation (19) [19, 21]:

$$N_{eff} = \rho \times \frac{N_A}{A}. \quad (19)$$

It also be expressed as equation 20:

$$N_{eff} = \frac{\frac{\mu}{\rho}}{\sigma_{t,el}} = \left(\frac{Z_{eff}}{M}\right) N_A \sum_i n_i, \quad (20)$$

where $f_i = \frac{n_i}{\sum_i n_i}$ and is the fractional elements present in the compound, n_i is the total number of atoms of the constituting element i, $\sum_i n_i$ is the total number of atoms present in the molecular formular, M is the molecular weight of the material.

Results and discussion

The radiation shielding parameters of metal oxide–based and oxide double perovskite ceramics are primarily governed by their density and were investigated to assess their suitability for radiation shielding applications. The obtained results were analyzed and discussed based on the influence of the three dominant photon–matter interaction mechanisms: photoelectric absorption, Compton scattering, and pair

production. Table 1 shows the chemical composition and densities of metal oxide-based and the oxide double perovskite samples.

Oxide-based Perovskite

Figure 1 shows the variations of MAC values as a function of photon energy in the range of 0.015–15 MeV. The MAC values for all samples decreased with increasing photon energy, particularly within the low-energy region from 0.015 to 0.03 MeV as shown in table 2. However, at 0.04 MeV, a noticeable increase in MAC values was observed for$BaTiO_3$ - ZrO_2 and $BaTiO_3$ -Mo, rising from 7.509 to 14.653 g/cm^2 and from 7.989 to 14.876 g/cm^2, respectively. This behavior is attributed to the K-absorption edges of the constituent elements, which occur at 0.018 MeV for Zr and 0.020 MeV for Mo. Since these K-edge energies lie just below 0.04 MeV, the photoelectric absorption increases sharply once the photon energy exceeds these thresholds, resulting in elevated MAC values. Beyond 0.04 MeV, $BaTiO_3$ - Mo consistently exhibited the highest MAC values, primarily due to the influence of Mo K-edge absorption. At low photon energies, photoelectric absorption dominates and is proportional to Z^3–Z^4; therefore, even small additions of high-Z elements can significantly enhance MAC values. In the intermediate energy region, where Compton scattering is the dominant interaction and depends mainly on electron density rather than atomic number, $BaTiO_3$ - Mo still shows slightly higher attenuation owing to its elemental composition. At higher photon energies, where pair production becomes significant and is proportional to Z^2, Mo continues to contribute more effectively than Zn or Zr. These observations indicate that atomic number and photon interaction mechanisms can, in some cases, play a more dominant role than material density. Consequently, $BaTiO_3$ – Mo emerges as the most effective radiation shielding material among the investigated samples. The incorporation of the high-Z dopant Mo enhances both photoelectric absorption and pair production interactions, making it a promising approach for improving radiation shielding performance in oxide-based perovskite ceramics.

Figure 2 shows the variation of LAC values with photon energy in the range of 0.015–15 MeV. In general, the LAC values decrease with increasing photon energy due to the transition of the dominant interaction mechanism from the photoelectric effect to Compton scattering and subsequently to pair production. At 0.04 MeV, a noticeable increase in LAC was observed for $BaTiO_3$ - Mo and $BaTiO_3$ - Mo, rising from

33.000 to 64.402 cm^{-1} and from 33.624 to 62.611 cm^{-1}, respectively as shown in table 3. This sharp increase is attributed to the dominance of the photoelectric effect near the K-absorption edges of the constituent elements, where photon absorption rises significantly. It is also evident that even when the material density is relatively low, a high mass attenuation coefficient (MAC) at a specific energy can result in a sharp increase in LAC. Beyond 0.04 MeV, $BaTiO_3$ - ZrO_2 consistently exhibited the highest LAC values. This behavior is associated with the incorporation of Zr, which provides a balanced and effective atomic number structure for photon interaction. Since LAC depends on both atomic number and material density, while MAC has a stronger influence over a wide energy range, these factors collectively govern the observed attenuation behavior. In the intermediate energy region, the differences in LAC values became less pronounced, particularly between $BaTiO_3$ - ZrO_2 and $BaTiO_3$ - Mo. At higher photon energies and across the overall energy range, both $BaTiO_3$ - ZrO_2 and $BaTiO_3$ - Mo maintained the highest LAC values, indicating their superior effectiveness as photon radiation shielding materials compared to the other investigated samples.

Figure 3 shows the variation of HVL values with photon energy in the range of 0.015–15 MeV. Overall, the HVL values increase with increasing photon energy for all samples, indicating reduced attenuation efficiency at higher energies. However, at 0.04 MeV, $BaTiO_3$ - ZrO_2 and $BaTiO_3$ - Mo exhibited a reduction in HVL values, decreasing from 0.021 to 0.011 cm and from 0.021 to 0.011 cm, respectively. This decrease is attributed to enhanced photon absorption associated with the photoelectric effect near the K-absorption edges of the high-Z dopant elements. Lower HVL values indicate better radiation attenuation performance, as a smaller material thickness is required to reduce the incident radiation intensity by 50% [23]. Since the photoelectric effect strongly depends on the atomic number ($\propto Z^4$ - Z^5), samples containing high-Z dopants demonstrate superior shielding efficiency and consequently exhibit lower HVL (and TVL) values [13,14]. In the low-energy region, where the photoelectric effect is dominant, $BaTiO_3$ - ZrO_2 showed higher attenuation efficiency, reflected by its lower HVL values. Moreover, this sample maintained relatively low HVL values in the intermediate and high-energy regions, confirming its effectiveness as a photon radiation shielding material across a wide energy range.

Figure 4 shows the variation of TVL values with photon energy in the range of 0.015–15 MeV. In general, the TVL values increase with increasing photon energy for all samples, indicating reduced shielding efficiency at higher energies. However, at 0.04 MeV, $BaTiO_3$ - ZrO_2 and $BaTiO_3$ - Mo exhibited a decrease in TVL values, with reductions from 0.070 to 0.036 cm and from 0.068 to 0.037 cm, respectively. This behavior is attributed to enhanced photon absorption near the K-absorption edges of the high-Z dopant elements.

Lower TVL values correspond to better radiation attenuation performance, as a smaller material thickness is required to reduce the incident radiation intensity by 90% [23]. Since the photoelectric effect strongly depends on the atomic number ($\propto Z^4$ - Z^5), samples containing high-Z dopants demonstrate superior shielding capability and consequently exhibit lower TVL values [13,14]. In the intermediate energy region, where Compton scattering is dominant and attenuation depends primarily on electron density, $BaTiO_3$ - ZrO_2 maintained the lowest TVL values, which can be attributed to its higher linear attenuation coefficient (LAC). Furthermore, at higher photon energies, where pair production becomes significant and its probability increases with Z^2, $BaTiO_3$ - ZrO_2 continued to exhibit the lowest TVL values, confirming its effectiveness as a radiation shielding material across the entire energy range.

Figure 5 shows the variation of MFP values with photon energy in the range of 0.015–15 MeV. In general, the MFP increases with increasing photon energy for all samples. However, at 0.04 MeV, $BaTiO_3$ - ZrO_2 and $BaTiO_3$ - Mo exhibited a decrease in MFP values, reducing from 0.030 to 0.0155 cm and from 0.030 to 0.0159 cm, respectively. $BaTiO_3$ - ZrO_2 consistently exhibited the lowest MFP values across the low-, intermediate-, and high-energy regions, indicating that photons travel the shortest average distance before interacting with the material. Consequently, $BaTiO_3$ - ZrO_2 requires less material thickness to attenuate radiation effectively, confirming its superior photon shielding performance compared to the other samples.

In summary, metal oxide–based perovskite samples exhibited strong photon attenuation capabilities, particularly in the low-energy region where the photoelectric effect is dominant. The incorporation of high-atomic-number (high-Z) metal oxides such as ZrO_2 and Mo, significantly enhanced both the MAC and LAC values by increasing the probability of photon interactions. Consequently, these high-Z doped perovskites displayed lower half-value layer HVL, TVL, and MFP values, indicating

superior radiation shielding efficiency. These results demonstrate that careful selection and incorporation of high-Z metal oxides into perovskite structures is an effective approach for optimizing photon attenuation performance in oxide-based perovskite ceramics.

Oxide Double-Perovskite Ceramics

Figure 6 shows MAC values with photon energy in the range of 0.015–15 MeV for the oxide double perovskite materials. In the low-energy region, the MAC values were generally higher, particularly for samples containing heavier elements (high-Z), which exhibited extremely high values, peaking at 0.015 MeV and decreasing rapidly with increasing energy. Ba_2FeReO_6 displayed the highest MAC values due to the presence of Re (Z = 75), which enhances photoelectric absorption. In contrast, Ba_2NaNbO_6 recorded the lowest MAC values because it contains lighter elements (Na and Nb), making it less effective for photon shielding. At 0.04 MeV, all samples exhibited a sharp rise in MAC values from 12.439 to 14.767, 10.788 to 16.276, 13.545 to 16.132, 8.123 to 15.658 and 7.860 to 15.611 respectively g/cm^2as shown in table 4. This attributed to the K-absorption edges of the constituent elements, whose energies lie just below 0.04 MeV. As the photon energy crosses these thresholds, the photoelectric effect increases sharply, resulting in elevated MAC values. In the intermediate-energy region, where Compton scattering is the dominant interaction, MAC values stabilized, leading to a narrower difference between the samples and generally lower attenuation. At high photon energies, where pair production becomes significant, MAC values were generally low for all samples (0.038, 0.037, 0.037, 0.037 and 0.037 g/cm^2 respectively). However, materials containing heavier elements continued to contribute slightly to attenuation, though not as strongly as in the low-energy region. Samples such as La_2NiMnO_6, La_2FeMnO_6 and Ba_2YMoO_6 exhibited moderate MAC values across the entire energy range, with no pronounced edge features. Overall, Ba_2FeReO_6 demonstrated superior MAC values across all energy regions, indicating its suitability for both low-energy X-ray and high-energy gamma-ray applications, and confirming its enhanced photon attenuation capability.

Figure 7 shows the variation of LAC values with photon energy in the range of 0.015–15 MeV for the oxide double perovskite materials. In the low-energy region, dominated by the photoelectric effect, LAC values decreased sharply as photon energy increased. However, at 0.04 MeV, all samples exhibited a sharp rise in LAC

from 93.168 to 110.604, 60.953 to 91.962, 80.996 to 96.468, 55.966 to 107.883, 53.291 to 105.843 respectively as shown in table 5. This is attributed to the K-absorption edges of the constituent elements, whose energies lie just below 0.04 MeV. As Compton scattering became the dominant interaction—depending primarily on electron density and material density—LAC values gradually decreased, and the differences between samples narrowed. Nevertheless, Ba_2FeReO_6 maintained slightly higher LAC values due to its high density (7.49 g/cm³) and the presence of heavy elements. In the high-energy region, LAC values continued to decrease, but samples with high density and high-Z elements still performed better, reflecting significant photoelectric interaction at low energies and notable pair production at higher energies. Consequently, Ba_2NaNbO_6 exhibited low attenuation across the entire energy range due to the incorporation of light atoms such as Na (Z = 11). La_2NiMnO_6 and La_2FeMnO_6, containing Mn, Fe, Ni, and La (Z = 57), provided moderate attenuation and are effective for shielding in the intermediate-energy region dominated by Compton scattering. Overall, Ba_2FeReO_6 consistently demonstrated superior photon attenuation performance across all energy levels.

Figure 8 shows the variation of HVL values with photon energy in the range of 0.015–15 MeV. At 0.015 MeV, the HVL values were generally low due to the strong photoelectric effect, with Ba_2FeReO_6 exhibiting the lowest HVL value (0.001 cm). This indicates the strongest photon attenuation capability at low photon energies and suggests suitability for a broad spectrum of photon energies. In contrast, Ba_2NaNbO_6 recorded the highest HVL (0.002 cm), making it the least effective sample for shielding. At 1.5 MeV, where Compton scattering is the dominant interaction, Ba_2FeReO_6 continued to show the lowest HVL value (1.909 cm), while Ba_2NaNbO_6 recorded the highest HVL (2.580 cm), confirming its relatively poor shielding capacity. At 15 MeV, where pair production becomes significant, HVL values increased for all samples; however, Ba_2FeReO_6 still demonstrated superior performance due to the presence of the high-Z element Re (Z = 75). Overall, Ba_2FeReO_6 consistently exhibited the lowest HVL values across the entire energy range, confirming it as the most effective photon shielding material among the studied perovskites.

Figure 9 shows the variation of TVL values with photon energy in the range of 0.015–15 MeV. In the low-energy region, dominated by the photoelectric effect and influenced by high material density, Ba_2FeReO_6 exhibited the lowest TVL values. As

Compton scattering became the dominant interaction—where both atomic number and density play a significant role—Ba_2FeReO_6 continued to maintain the lowest TVL values, followed closely by La_2NiMnO_6 and La_2FeMnO_6. In contrast, Ba_2NaNbO_6 displayed the highest TVL values, resulting in the ranking: Ba_2FeReO_6 < La_2NiMnO_6 < La_2FeMnO_6 < Ba_2YMoO_6 < Ba_2NaNbO_6. Furthermore, in the high-energy region, where pair production becomes significant, Ba_2FeReO_6 retained the lowest TVL values across all energy levels, demonstrating its superior photon shielding capability.

Figure 10 shows the MFP values with photon energy in the range of 0.015–15 MeV. Ba_2FeReO_6 consistently exhibited the lowest MFP values across all energy levels due to the presence of the high-Z Re element and its high density. La_2NiMnO_6 and La_2FeMnO_6 also showed relatively low MFP values, attributable to the presence of La and other transition metals. In the intermediate-energy region, where density plays a major role, Ba_2FeReO_6 continued to maintain the lowest MFP values, followed closely by La_2NiMnO_6 and La_2FeMnO_6 due to their comparatively high densities. At higher energies, where pair production becomes the dominant interaction, dense and high-Z samples demonstrated better attenuation. Overall, the MFP values increased with photon energy for all samples as a result of the decreasing probability of photon interactions.

In summary, the shielding performance of oxide double perovskite ceramics is strongly influenced by their compositional complexity, density, and the presence of heavy transition metals such as Re, Mo, Nb, and Fe. Among the studied materials, samples containing higher-Z and higher-density constituents exhibited enhanced MAC and LAC values across the investigated energy range. This resulted in lower HVL, TVL and MFP values, demonstrating improved photon attenuation efficiency. The structural flexibility of double perovskites allows for effective elemental substitution, making them promising candidates for advanced radiation shielding applications. Comparative analysis between the two perovskite families showed that oxide double perovskite ceramics generally outperform metal oxide–based perovskites, particularly in the intermediate- and high-energy regions where Compton scattering and pair production dominate. This superior performance can be attributed to their higher effective atomic numbers, increased density, and complex crystal structures, which collectively enhance photon–matter interactions.

Conclusion

In this study, the photon attenuation properties of metal oxide–based and oxide double perovskites were investigated using Phy-X/PSD and NGCal software over an energy range of 0.015–15 MeV. The results, based on the total interaction cross-section contributions of photon–matter interactions, show that all investigated samples exhibit higher attenuation efficiency in the low-energy region due to the dominance of the photoelectric effect, followed by a gradual reduction in shielding performance at intermediate and high energies, where Compton scattering and pair production are dominant. Materials containing higher-Z and higher-density constituents demonstrated superior shielding performance, reflected by increased MAC and LAC values and reduced HVL, TVL, and MFP values. The radiation shielding parameters obtained from the two software tools were in excellent agreement, with discrepancies within 0.1%. For metal oxide–based perovskite samples, strong photon attenuation was particularly observed in the low-energy region dominated by the photoelectric effect. Incorporating high-atomic-number (high-Z) metal oxides such as ZrO_2, and Mo, significantly enhanced MAC and LAC values due to increased photon interaction probabilities, resulting in lower HVL, TVL, and MFP values and indicating superior shielding efficiency. In the case of oxide double perovskite ceramics, shielding performance was strongly influenced by compositional complexity, density, and the presence of heavy transition metals such as Re, and Mn. Samples containing higher-Z and higher-density constituents exhibited enhanced MAC and LAC values across the entire energy range, accompanied by reduced HVL, TVL, and MFP values, highlighting their improved photon attenuation efficiency. The structural flexibility of double perovskites allows for effective elemental substitution, making them promising candidates for advanced radiation shielding applications. A comparative assessment between the two perovskite families revealed that oxide double perovskite ceramics generally outperform metal oxide–based perovskites, particularly at intermediate and high photon energies where Compton scattering and pair production dominate. This enhanced performance is attributed to their higher effective atomic numbers, increased density, and complex crystal structures, which collectively promote stronger photon–matter interactions. Therefore, based on this comprehensive evaluation, oxide double perovskites are recommended as more efficient photon shielding materials than metal oxide–based perovskite composites, owing to their higher attenuation capability and lower penetration depth requirements. Future work should focus on experimental validation of these theoretical results, as well as investigations into

mechanical strength, thermal stability, and radiation durability to assess practical applicability.

References

[1] Mahdi, R.I., Hanfi, M.Y., Mhareb, M.H.A., Sayyed, M.I. Kadhim, A.J., Kaky, K.M.; Transparent heavy-metal glass-ceramics reinforced with nano-PbO for next-generation X- and γ-ray shielding applications. *Material Research Bulletin*, 195, (2025). https://doi.org/10.1016/j.materresbull.2025.113808.

[2] Alawaideh, S.E., Sayyed, M. I., Mahmoud, K. A., Hanfi, M.Y., Imheidat, M.A., Kaky, K.M., Thabit, H.A., Elsafi, H.; Effect of different metal oxides on the Radiation shielding features of borate glasses. *Radiation Physics and Chemistry,* 220, (2024). https://doi.org/10.1016/j.radphyschem.2024.111720.

[3] Sayyed, M. I., Zaiter, M.J., Mhareb, M.H.A, Mahmoud, K.A., Biradar, S., Mahdi, R.I., Kaky, K.M.; Optical, physical, mechanical, structural, and radiation shielding investigations of B_2O_3–TeO_2-GeO_2-MgO-PbO for ionizing protection and optical transmission application. *Optical Materials,* 154, (2024). https://doi.org/10.1016/j.optmat.2024.115807.

[4] Okonkwo U.C., Idumah C.I., Okafor C.E., Ohagwu C.C., Aronu M.E., Okokpujie I.P., Chukwu N.N., Chukwunyelu C.E.; Development, Characterization, and Properties of Polymeric Nanoarchitectures for Radiation Attenuation. *Journal of Inorganic and Organometallic Polymers and Materials*, *32*(11), 4093-4113 (2022) https://doi.org/10.1007/s10904-022-02420-y.

[5] More C.V., Alsayed Z., Badaw M.S., Thabet A.A., Pawar P.P.; Polymeric composite materials for radiation shielding: a review. In *Environmental Chemistry Letters* 19(3), 2057-2090 (2021). https://doi.org/10.1007/s10311-021-01189-9.

[6] Hannachi E., Mahmoud K.G., Slimani Y., Sayyed M.I., Arayro J., Maghrbi Y.; Monte Carlo Simulation for Investigating the Sintering Temperatures Effects on Radiation Shielding Performances of Lead-Free ABO_3 Perovskite Ceramic. *Crystals*, 13(2), 1-14 (2023). https://doi.org/10.3390/cryst13020230.

[7] Amini M., Vejdani-Noghreyian A., Ebrahimi-Khankook A., Khorsand-Zak A., Bakaiyan M.; Experimental and Theoretical Study of Gamma-Ray Attenuation Properties of $PbCu_3$ Ti_4O_{12} Ceramic. In *Romanian Journal of Physics* (67), 303 (2022).

[8] Hannachi E., Mahmoud K.A., Sayyed M.I., Slimani Y. Structure, optical properties, and ionizing radiation shielding performance using Monte Carlo simulation for lead-free BTO perovskite ceramics doped with ZnO, SiO2, and WO3 oxides. *Materials Science in Semiconductor Processing*, 145 (2022). https://doi.org/10.1016/j.mssp.2022.106629.

[9] Slimani Y., Hamad M.K., Olarinoye I.O., Alajerami Y.S., Sayyed M.I., Almessiere M.A., Mhareb M.H.A.; Determination of structural features of different Perovskite ceramics and investigation of ionizing radiation shielding properties. *Journal of Materials Science: Materials in Electronics*, 32(15), 20867-20881(2021). https://doi.org/10.1007/s10854-021-06603-0.

[10] Jreije A., Mutyala S.K., Urbonavičius B.G., Šablinskaitė A., Keršienė N., Puišo J., Rutkūnienė Ž., Adlienė Ž. D.; Modification of 3D Printable Polymer Filaments for Radiation Shielding Applications. *Polymers*, 15(7), 1-17 (2023). https://doi.org/10.3390/polym15071700.

[11] Assirey E. A. R.; Perovskite synthesis, properties and their related biochemical and industrial application. In *Saudi Pharmaceutical Journal* 27(6), 817-829 (2019) https://doi.org/10.1016/j.jsps.2019.05.003.

[12] Sharma A., Singh B., Sandhu, B.S.; Investigation of photon interaction parameters of polymeric materials using Monte Carlo simulation. *Chinese Journal of Physics*, 60, 709-719 (2019b). https://doi.org/10.1016/j.cjph.2019.06.011.

[13] Hadil K.; Theoretical investigation of gamma shielding of new Perovskites. A thesis submitted to the Department of Physics, Faculty of Mathematics and Material Science Field of Material Science, Kasdi Merbah University Ouargla, 1-77 (2024).

[14] Şakar E., Alim B., Fırat Ö. Ö., Ceviz S.B., Baltakesmez A., Akbaba U.; A surveying of photon and particle radiation interaction characteristics of some perovskite materials. *Radiation Physics and Chemistry*, 189, 1-10 (2021). https://doi.org/10.1016/j.radphyschem.2021.109719.

[15] Gökçe H.S., Güngör O., Yilmaz H.; An online software to simulate the shielding properties of materials for neutron and photons: NGCal. *Radiation Physics and Chemistry*, 185, 1-6 (2021).

https://doi.org/10.1016/j.radphyschem.2021.109519.

[16] Khan N., Rooh G., Mukamil S., Khattak S.A., Shoaib M., Khan I., Ullah I., Ahmad T., Shah S.K., Safeen K., Shoaib M.; Radiation shielding performance of tellurium–thallium and tellurium–lead oxide glass systems. *Radiation Physics and Chemistry,* 217, 1-10 (2024).
https://doi.org/10.1016/j.radphyschem.2024.111517.

[17] Sharma A., Nazrin S.N., Humaira S.A., Boukhris I., Kebaili I.; Impact of neodymium oxide on optical properties and X-ray shielding competence of Nd_2O_3–TeO_2–ZnO glasses. *Radiation Physics and Chemistry* 195*,* 1-10 (2022).
https://doi.org/10.1016/j.radphyschem.2022.110047.

[18] Olukotun S.F., Gbenu S.T., Oladejo O.F., Sayyed M.I., Tajudin S.M., Amosun A.A., Fadodun O.G., Fasasi M.K.; Investigation of gamma ray shielding capability of fabricated clay-polyethylene composites using EGS5, XCOM and Phy-X/PSD. *Radiation Physics and Chemistry*, 177, 1-8 (2020).
https://doi.org/10.1016/j.radphyschem.2020.109079.

[19] Sharma A., Sayyed M.I., Agar O., Tekin H.O.; Simulation of shielding parameters for TeO_2-WO_3-GeO_2 glasses using FLUKA code. *Results in Physics*, 13, 1-8 (2019a).
https://doi.org/10.1016/j.rinp.2019.102199.

[20] Hannachi E., Sayyed M.I., Mahmoud K.A., Slimani Y., Akhtar S., Albarzan B., Almuqrin A.H.; Impact of tin oxide on the structural features and radiation shielding response of some ABO_3 perovskites ceramics (A = Ca, Sr, Ba; B = Ti). *Applied Physics A: Materials Science and Processing*, *127*(12), 1-12 (2021).
https://doi.org/10.1007/s00339-021-05092-6.

[21] Mohammed M.1., Yahia I.S. Zahran H.Y.; Radiation attenuation parameters of $Ti3SiC_2$ MAX phase and their binary compounds using Phy-X/PSD software. *Materials Science in Semiconductor Processing*, 169, 1-8 (2024).
https://doi.org/10.1016/j.mssp.2023.107916.

[22] Olaosun A., Aborisade C., Shian D., Oloyede O., Osuolale P.; Comprehensive Study of Photon and Proton Interactions to Interpret the Radiation Parameters of Boron Derivative Drugs for Chemoradiotherapy. *Journal of Nigerian Society of Physical Science,* 7, 1-13 (2025).
https:/doi.org/10.46481/jnsps.2025.2503.

[23] Alzahrani J. S., Sharma A., Nazrin S. N., Alrowaili Z. A., Al-Buriahi, M. S.; Optical and radiation shielding effectiveness of a newly fabricated WO3 doped TeO2–B2O3 glass system. *Radiation Physics and Chemistry*, 193 (2022). https://doi.org/10.1016/j.radphyschem.2022.109968.

[24] Donya H., Sulami S.; Photon Shielding Characterization of a Modified Titania-Bismuth-Borotellurite Glass System for Medical Applications. *Journal of the Korean Physical Society*, 75(11), 871-877 (2019). 10.3938/jkps.75.871.

[24] Nazrin S.N., Sharma A., Muhammad S., Ighamdi N.A., Wageh S.; Mechanical and radiation shielding properties of CuO doped TeO_2–B_2O_3 glass system. *Radiation Physics and Chemistry*, 198, 1-11 (2022). https://doi.org/10.1016/j.radphyschem.2022.110222.

Table 1: Chemical composition and densities of metal oxide-based and the oxide double perovskite samples.

Chemical formula	Density (gcm^{-3})	Chemical formula	Density (gcm^{-3})
$BaTiO_3$- ZrO_2	4.395	Ba_2FeReO_6	7.49
$BaTiO_3 - Mo$	4.209	Ba_2NaNbO_6	5.65
$SrMnO_3$-TeO_2	4.442	Ba_2YMoO_6	5.98
$SrMnO_3$- ZnO	4.192	La_2NiMnO_6	6.89
		La_2FeMnO_6	6.78

Table 2: MAC values for metal oxide-based perovskite samples

Energy (MeV)	$BaTiO_3 - ZrO_2$ Phy-X/PSD	NGCal	$BaTiO_3 - Mo$ Phy-X/PSD	NGCal	$SrMnO_3 - TeO_2$ Phy-X/PSD	NGCal	$SrMnO_3 - ZnO$ Phy-X/PSD	NGCal
0.015	43.793	43.798	44.284	44.289	25.339	25.338	26.569	26.568
0.02	22.386	22.387	23.673	23.724	35.217	35.218	35.775	35.776
0.03	7.509	7.509	7.989	7.989	11.783	11.787	11.953	11.957
0.04	14.653	14.652	14.876	14.874	6.046	6.046	5.436	5.437
0.05	8.223	8.224	8.344	8.345	3.298	3.298	2.956	2.957
0.06	5.089	5.089	5.162	5.162	2.023	2.023	1.812	1.812
0.08	2.395	2.395	2.427	2.427	0.964	0.964	0.868	0.868
0.1	1.349	1.350	1.366	1.367	0.568	0.568	0.516	0.516
0.15	0.512	0.512	0.518	0.518	0.257	0.257	0.241	0.241
0.2	0.286	0.286	0.288	0.288	0.172	0.172	0.165	0.165
0.3	0.153	0.153	0.154	0.154	0.117	0.117	0.115	0.115
0.4	0.112	0.112	0.112	0.112	0.096	0.096	0.096	0.096
0.5	0.093	0.093	0.093	0.093	0.085	0.085	0.084	0.084
0.6	0.081	0.081	0.081	0.081	0.077	0.077	0.077	0.077
0.8	0.068	0.068	0.068	0.068	0.066	0.066	0.066	0.066
1	0.059	0.059	0.059	0.059	0.059	0.059	0.059	0.059
1.5	0.048	0.048	0.048	0.048	0.048	0.048	0.048	0.048
2	0.042	0.042	0.042	0.042	0.042	0.042	0.042	0.042
3	0.036	0.036	0.036	0.036	0.036	0.036	0.036	0.036
4	0.034	0.034	0.034	0.034	0.033	0.033	0.033	0.033
5	0.033	0.033	0.033	0.033	0.031	0.031	0.031	0.031
6	0.033	0.033	0.033	0.033	0.030	0.030	0.030	0.030
8	0.033	0.033	0.033	0.033	0.029	0.029	0.029	0.029
10	0.034	0.034	0.034	0.034	0.030	0.030	0.029	0.029
15	0.036	0.036	0.036	0.036	0.031	0.031	0.030	0.030

Table 3: LAC values for metal oxide-based perovskite samples

Energy (MeV)	$BaTiO_3 - ZrO_2$ Phy-X/PSD	$BaTiO_3 - ZrO_2$ NGCal	$BaTiO_3 - Mo$ Phy-X/PSD	$BaTiO_3 - Mo$ NGCal	$SrMnO_3 - TeO_2$ Phy-X/PSD	$SrMnO_3 - TeO_2$ NGCal	$SrMnO_3 - ZnO$ Phy-X/PSD	$SrMnO_3 - ZnO$ NGCal
0.015	192.470	192.490	186.393	186.412	112.554	112.549	111.378	111.373
0.02	98.385	98.389	99.638	99.852	156.434	156.437	149.970	149.971
0.03	33.000	33.002	33.624	33.627	52.341	52.359	50.107	50.124
0.04	64.402	64.397	62.611	62.606	26.854	26.857	22.789	22.793
0.05	36.142	36.145	35.120	35.122	14.648	14.650	12.392	12.394
0.06	22.367	22.366	21.726	21.725	8.987	8.987	7.598	7.598
0.08	10.526	10.525	10.216	10.215	4.283	4.283	3.638	3.637
0.1	5.931	5.932	5.751	5.752	2.524	2.524	2.164	2.164
0.15	2.252	2.252	2.179	2.179	1.143	1.143	1.010	1.009
0.2	1.257	1.257	1.213	1.213	0.763	0.763	0.690	0.690
0.3	0.674	0.674	0.648	0.648	0.519	0.519	0.481	0.481
0.4	0.493	0.493	0.473	0.473	0.428	0.428	0.400	0.400
0.5	0.408	0.408	0.391	0.391	0.377	0.377	0.354	0.354
0.6	0.358	0.358	0.343	0.343	0.342	0.342	0.322	0.322
0.8	0.298	0.298	0.285	0.285	0.295	0.295	0.278	0.278
1	0.261	0.261	0.250	0.250	0.263	0.263	0.248	0.248
1.5	0.209	0.209	0.200	0.200	0.213	0.213	0.202	0.202
2	0.184	0.184	0.176	0.176	0.186	0.186	0.176	0.176
3	0.160	0.160	0.153	0.153	0.158	0.158	0.149	0.149
4	0.150	0.150	0.144	0.144	0.145	0.145	0.137	0.137
5	0.145	0.145	0.140	0.140	0.138	0.138	0.130	0.130
6	0.144	0.144	0.138	0.138	0.134	0.134	0.126	0.126
8	0.144	0.144	0.139	0.139	0.131	0.131	0.123	0.123
10	0.148	0.148	0.142	0.142	0.131	0.131	0.123	0.123
15	0.158	0.158	0.153	0.153	0.136	0.136	0.126	0.126

Table 4: MAC values for oxide double perovskite samples

Energy (MeV)	Ba_2FeReO_6		Ba_2NaNbO_6		Ba_2YMoO_6		La_2NiMnO_6		La_2FeMnO_6	
	Phy-X/PSD	NGCal	Phy-X/PSD	NGCal	Phy-X/PSD	NGCal	Phy-X/PSD	NGCal	Phy-X/PSD	NGCal
0.015	77.706	77.705	41.509	41.515	40.269	40.275	52.921	52.916	51.234	51.229
0.02	36.418	36.419	31.571	31.579	39.385	39.557	24.361	24.363	23.563	23.566
0.03	12.439	12.438	10.788	10.790	13.545	13.544	8.123	8.120	7.860	7.858
0.04	14.767	14.765	16.276	16.275	16.132	16.132	15.658	15.661	15.611	15.614
0.05	8.279	8.280	9.107	9.108	8.992	8.993	8.781	8.780	8.759	8.758
0.06	5.131	5.132	5.623	5.623	5.538	5.538	5.446	5.447	5.434	5.435
0.08	4.310	4.309	2.632	2.632	2.585	2.584	2.561	2.561	2.556	2.557
0.1	2.436	2.437	1.475	1.476	1.446	1.447	1.442	1.441	1.439	1.439
0.15	0.888	0.888	0.552	0.552	0.541	0.541	0.544	0.544	0.543	0.543
0.2	0.461	0.461	0.303	0.303	0.298	0.298	0.301	0.301	0.300	0.300
0.3	0.213	0.213	0.159	0.159	0.156	0.156	0.159	0.159	0.158	0.158
0.4	0.140	0.140	0.115	0.114	0.113	0.113	0.115	0.115	0.115	0.115
0.5	0.109	0.109	0.094	0.094	0.093	0.093	0.095	0.095	0.094	0.094
0.6	0.091	0.091	0.082	0.082	0.081	0.081	0.083	0.083	0.083	0.083
0.8	0.072	0.072	0.068	0.068	0.067	0.067	0.069	0.069	0.068	0.068
1	0.062	0.062	0.059	0.059	0.059	0.059	0.060	0.060	0.060	0.060
1.5	0.048	0.048	0.048	0.048	0.047	0.047	0.048	0.048	0.048	0.055
2	0.043	0.043	0.042	0.042	0.042	0.042	0.042	0.042	0.042	0.042
3	0.038	0.038	0.037	0.037	0.037	0.037	0.037	0.037	0.037	0.037
4	0.036	0.036	0.035	0.035	0.035	0.035	0.035	0.035	0.035	0.035
5	0.036	0.036	0.034	0.034	0.034	0.034	0.034	0.034	0.034	0.034
6	0.036	0.036	0.034	0.034	0.034	0.034	0.033	0.033	0.033	0.033
8	0.037	0.037	0.034	0.034	0.034	0.034	0.034	0.034	0.034	0.034
10	0.039	0.039	0.035	0.035	0.036	0.036	0.035	0.035	0.034	0.034
15	0.043	0.043	0.038	0.038	0.039	0.038	0.037	0.037	0.037	0.037

Table 5: LAC values for oxide double perovskite samples

Energy (MeV)	Ba_2FeReO_6		Ba_2NaNbO_6		Ba_2YMoO_6		La_2NiMnO_6		La_2FeMnO_6	
	Phy-X/PSD	NGCal	Phy-X/PSD	NGCal	Phy-X/PSD	NGCal	Phy-X/PSD	NGCal	Phy-X/PSD	NGCal
0.015	582.018	582.009	234.524	234.559	240.807	240.847	364.627	364.594	347.369	347.333
0.02	272.771	272.775	178.379	178.421	235.519	236.552	167.845	167.864	159.759	159.777
0.03	93.168	93.158	60.953	60.964	80.996	80.996	55.966	55.947	53.291	53.275
0.04	110.604	110.587	91.962	91.952	96.468	96.471	107.883	107.902	105.843	105.862
0.05	62.008	62.014	51.456	51.462	53.774	53.778	60.504	60.495	59.386	59.377
0.06	38.435	38.436	31.768	31.768	33.117	33.119	37.524	37.529	36.842	36.847
0.08	32.279	32.276	14.873	14.873	15.456	15.455	17.647	17.648	17.333	17.334
0.1	18.246	18.250	8.336	8.338	8.649	8.651	9.932	9.931	9.757	9.756
0.15	6.648	6.648	3.118	3.118	3.233	3.234	3.746	3.746	3.680	3.680
0.2	3.451	3.451	1.713	1.713	1.780	1.780	2.072	2.072	2.035	2.035
0.3	1.596	1.596	0.896	0.896	0.935	0.935	1.093	1.093	1.073	1.073
0.4	1.051	1.051	0.647	0.647	0.677	0.677	0.793	0.793	0.778	0.778
0.5	0.814	0.814	0.531	0.531	0.557	0.557	0.653	0.653	0.640	0.640
0.6	0.683	0.683	0.464	0.464	0.487	0.487	0.570	0.570	0.559	0.559
0.8	0.542	0.542	0.384	0.384	0.404	0.404	0.473	0.473	0.464	0.438
1	0.463	0.463	0.336	0.336	0.353	0.353	0.414	0.414	0.406	0.406
1.5	0.363	0.363	0.269	0.269	0.283	0.283	0.331	0.331	0.325	0.375
2	0.320	0.320	0.236	0.236	0.249	0.249	0.291	0.291	0.285	0.285
3	0.284	0.284	0.207	0.207	0.219	0.219	0.254	0.254	0.249	0.249
4	0.272	0.272	0.195	0.195	0.207	0.207	0.239	0.239	0.234	0.234
5	0.269	0.270	0.191	0.191	0.203	0.203	0.233	0.232	0.228	0.228
6	0.271	0.271	0.189	0.189	0.202	0.202	0.231	0.230	0.226	0.226
8	0.279	0.279	0.192	0.192	0.206	0.206	0.233	0.233	0.228	0.228
10	0.290	0.290	0.197	0.197	0.212	0.212	0.239	0.239	0.233	0.233
15	0.318	0.318	0.213	0.213	0.230	0.230	0.257	0.257	0.251	0.251

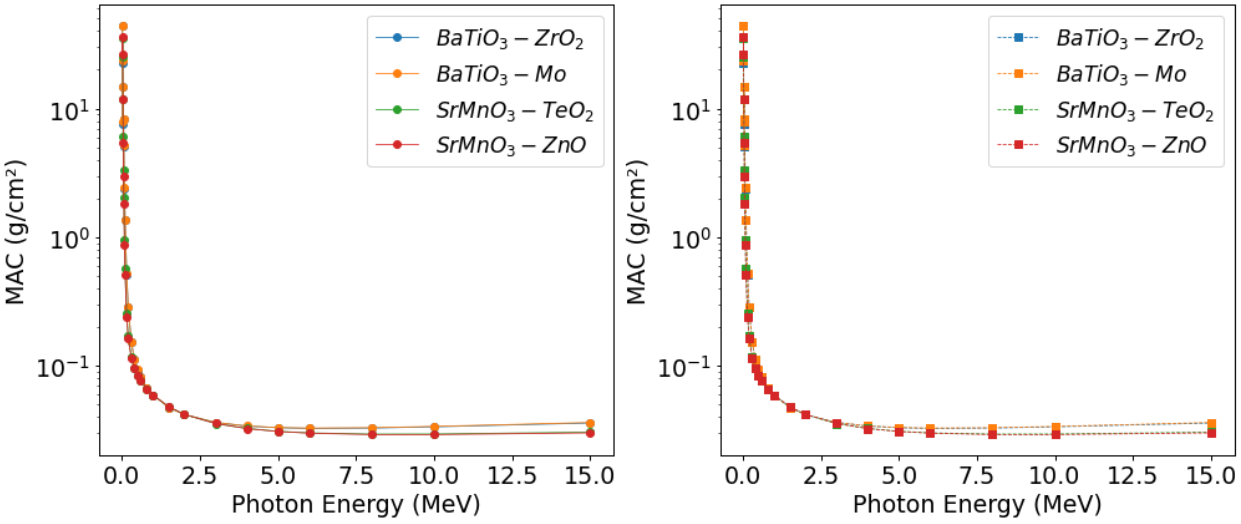

Figure 1: Variations of MAC values versus incident photon energy (0.015-15 MeV) of metal oxide-based perovskite for (a) PHY-X/PSD (b) NGCal Software.

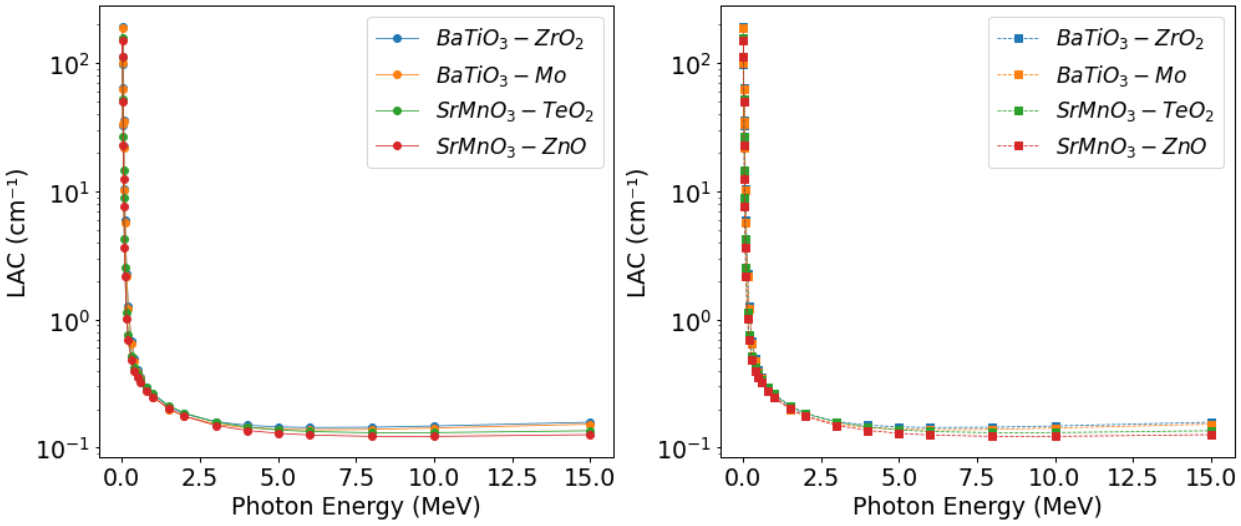

Figure 2: Variations of LAC values versus incident photon energy (0.015-15 MeV) of metal oxide-based perovskite for (a) PHY-X/PSD (b) NGCal Software.

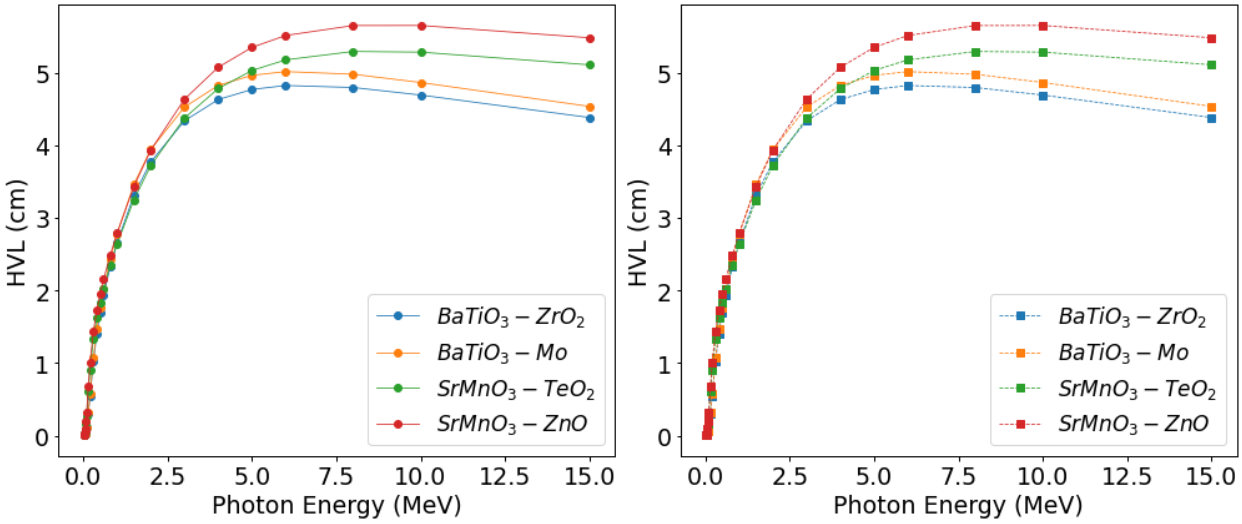

(a) (b)

Figure 3: Variations of HVL values versus incident photon energy (0.015-15 MeV) of metal oxide-based perovskite for (a) PHY-X/PSD (b) NGCal Software.

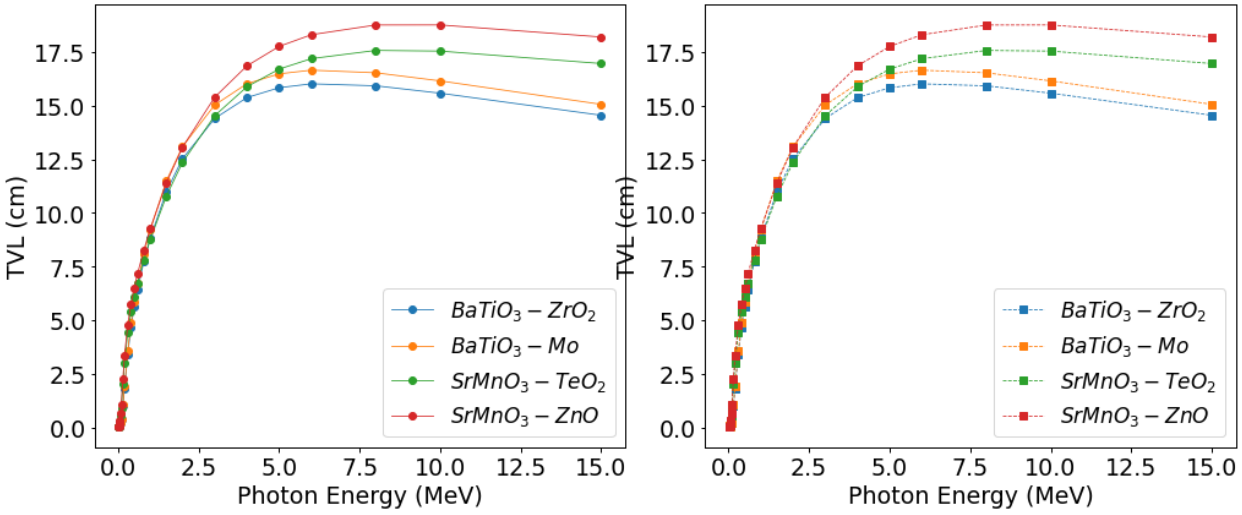

(a) (b)

Figure 4: Variation of TVL values versus incident photon energy (0.015-15 MeV) of metal oxide-based perovskite for (a) PHY-X/PSD (b) NGCal Software.

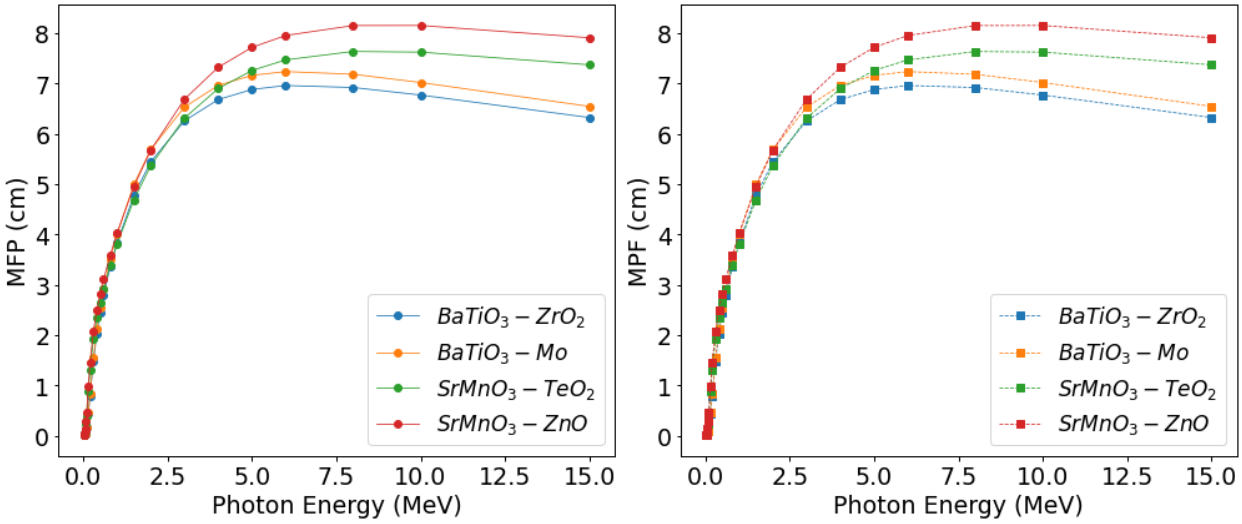

(a) (b)

Figure 5: Variations of MFP values versus incident photon energy (0.015-15 MeV) of metal oxide-based perovskite for (a) PHY-X/PSD (b) NGCal Software.

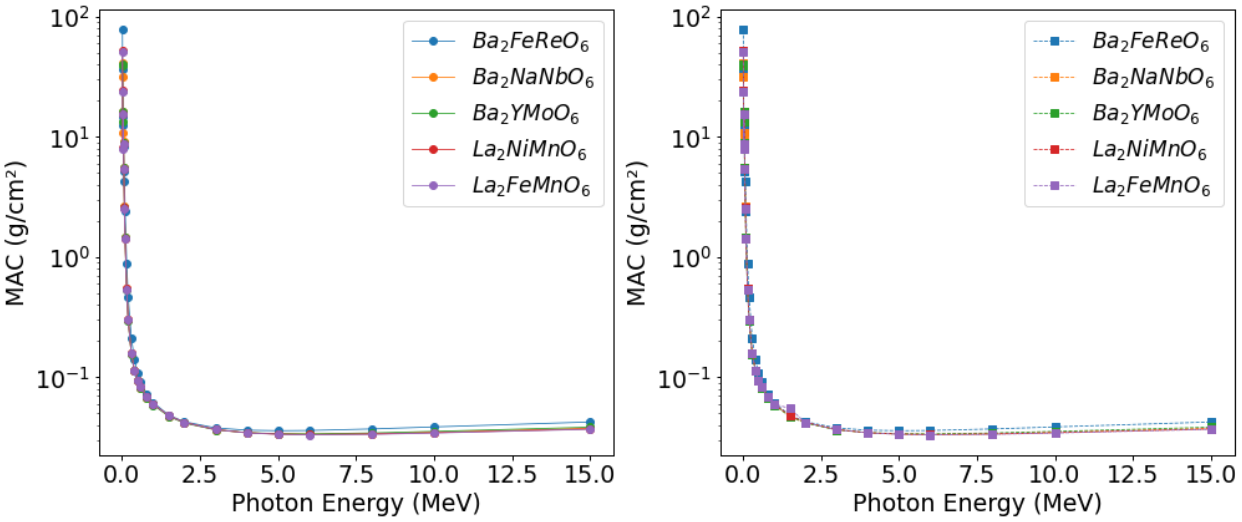

(a) (b)

Figure 6: Variations of MAC values versus incident photon energy (0.015-15 MeV) of oxide double-perovskite for (a) PHY-X/PSD (b) NGCal Software.

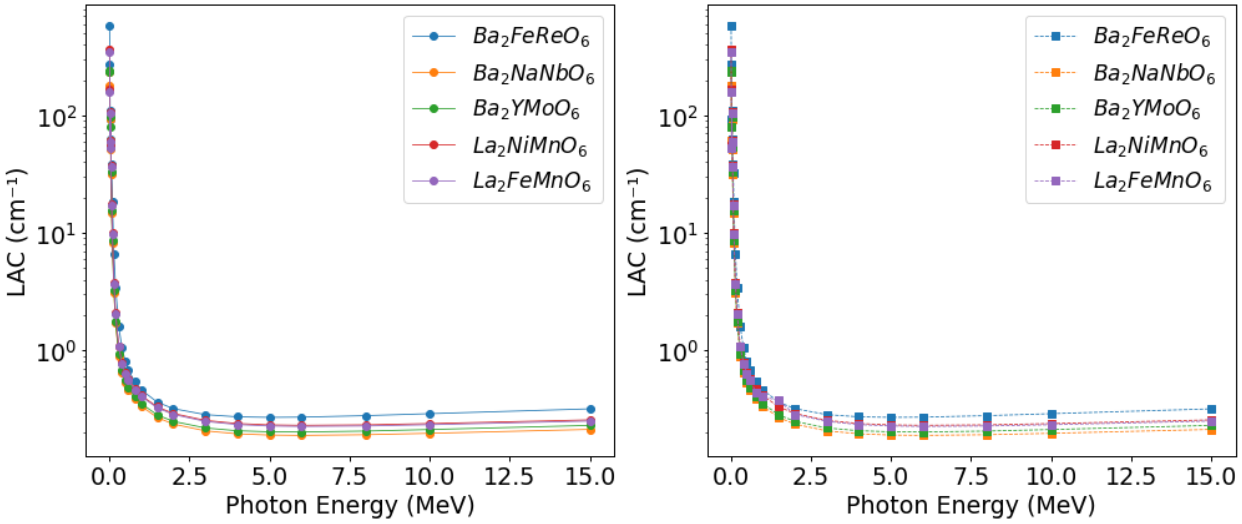

(a) (b)

Figure 7: Variation of LAC values versus incident photon energy (0.015-15 MeV) of oxide double-perovskite for (a) PHY-X/PSD (b) NGCal Software.

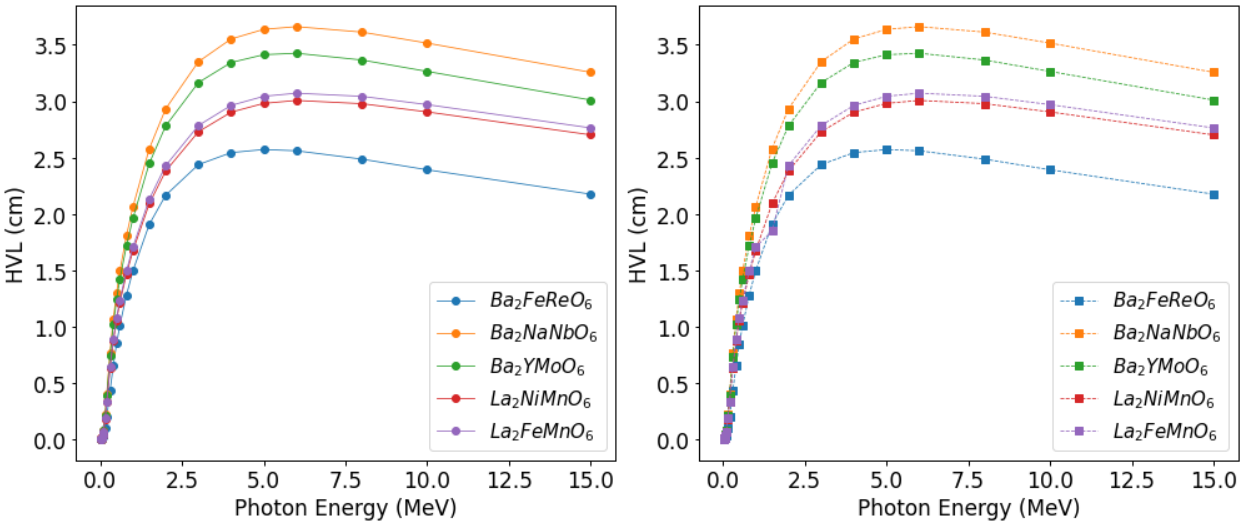

(a) (b)

Figure 8: The changes of HVL values versus incident photon energy (0.015-15 MeV) of oxide double-perovskite for (a) PHY-X/PSD (b) NGCal Software.

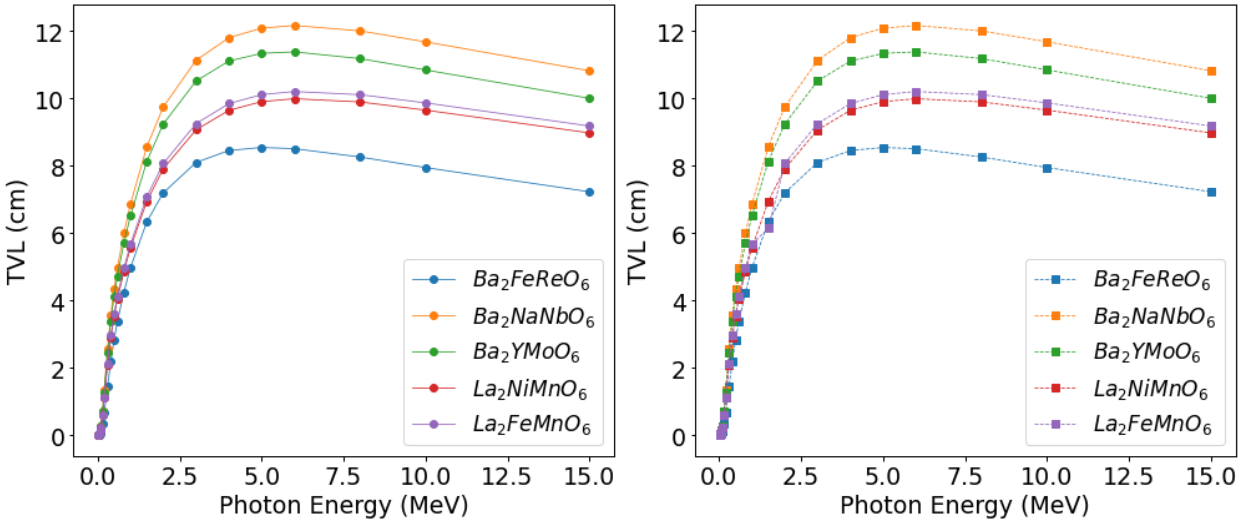

(a) (b)

Figure 9: The changes of TVL values versus incident photon energy (0.015-15 MeV) of oxide double-perovskite for (a) PHY-X/PSD (b) NGCal Software.

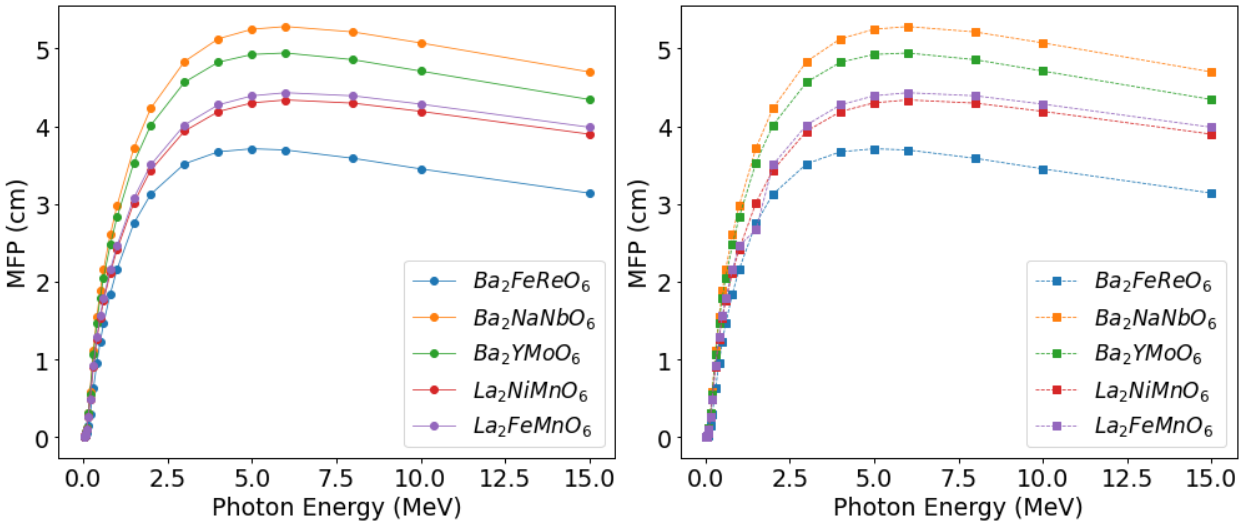

(a) (b)

Figure 10: The changes of MFP values versus incident photon energy (0.015-15 MeV) of oxide double-perovskite for (a) PHY-X/PSD (b) NGCal Software.

Declaration of source of found

No fund or grant was received for conducting this study.

Declaration of competing interest

The authors declare that they have no known competing financial interests or personal relationships that could have appeared to influence the work reported in this paper.

Author's contribution

Muhammed Aburraheem: conceptualization, data curation, formal analysis, investigation, methodology, project administration, resources, software, Validation, Visualization, Writing - original draft, **Sunday Ajani and Wasiu Yahya:** project administration, resources, software, supervision, validation, visualization, **Godwin Egbeyale:** writing – review, editing and finalizing the paper.

Data Availability

The raw data that support the findings are available on request from the corresponding author.